NASA TECHNICAL REPORT

NASA TR R-274

c. 1

NASA TR R-274

EXPERIMENTALLY DETERMINED LOCAL FLOW PROPERTIES AND DRAG COEFFICIENTS FOR A FAMILY OF BLUNT BODIES AT MACH NUMBERS FROM 2.49 TO 4.63

by Robert L. Stallings, Jr.

Langley Research Center
Langley Station, Hampton, Va.

NATIONAL AERONAUTICS AND SPACE ADMINISTRATION • WASHINGTON, D. C. • OCTOBER 1967

EXPERIMENTALLY DETERMINED LOCAL FLOW PROPERTIES AND DRAG COEFFICIENTS FOR A FAMILY OF BLUNT BODIES AT MACH NUMBERS FROM 2.49 TO 4.63

By Robert L. Stallings, Jr.

Langley Research Center
Langley Station, Hampton, Va.

NATIONAL AERONAUTICS AND SPACE ADMINISTRATION

For sale by the Clearinghouse for Federal Scientific and Technical Information
Springfield, Virginia 22151 – CFSTI price $3.00

EXPERIMENTALLY DETERMINED LOCAL FLOW PROPERTIES AND DRAG COEFFICIENTS FOR A FAMILY OF BLUNT BODIES AT MACH NUMBERS FROM 2.49 TO 4.63

By Robert L. Stallings, Jr.
Langley Research Center

SUMMARY

Drag coefficients and local flow properties were experimentally determined for a family of blunt bodies at Mach numbers from 2.49 to 4.63 at a Reynolds number, based on afterbody diameter, of 1.88×10^6. The family consisted of bodies of revolution having variable nose and shoulder radii (r_n and r_c, respectively) and cylindrical afterbodies 7.5 inches (191 mm) in diameter (d). The geometry of the 18 models tested ranged from a hemisphere-cylinder to a flat-face cylinder.

The Mach number effect on nondimensional pressure and velocity distributions of the hemispherical model decreased rapidly with increasing Mach number. These distributions at Mach number 4.63 were essentially the same as previously published results for Mach numbers up to 11.4. Increasing the nose bluntness also decreased the Mach number effect on the pressure and velocity distributions. There was no effect of Mach number on these distributions for the zero-shoulder-radius models for $\frac{r_n}{d} > 0.707$. Drag coefficients determined from integrated pressures over the nose of the hemispherical model and by assuming the base pressure coefficient to correspond to $-1/M_\infty^2$ (where M_∞ is the free-stream Mach number) were in good agreement with previously published data for a sphere. These results were also in good agreement with drag coefficients determined from modified Newtonian theory. A reduction in drag coefficients as indicated by both experiment and theory occurred for a decrease in bluntness obtained by an increase in shoulder radius. The maximum velocity gradient for all models occurred either at or slightly downstream of the point of tangency of the nose and shoulder arcs. Stagnation-point velocity gradients determined from measured pressures were in good agreement throughout the range of variables of this investigation with theoretical estimates based on Traugott's method and measured shock-standoff distances.

A comprehensive presentation of these data in figure form is included for sufficiently small intervals of nose and shoulder radii to enable the pressure distributions, velocity distributions, stagnation-point velocity gradients, shock-standoff distances, or drag coefficients to be determined – either directly or by interpolation – for any body of the general shape described. Since all these variables indicated only very small Mach number effects at the higher test Mach numbers, these results should be applicable at a much higher range of Mach number than that of this investigation.

INTRODUCTION

The advantages of blunt nose shapes for reducing the convective aerodynamic heating at the forward stagnation point of bodies moving at hypersonic flight speeds have been well established within the past decade. Unfortunately, the governing partial-differential equations for the subsonic flow field between the bow shock wave and nose of such bodies are of the elliptic type and, as yet, no exact analytical solutions are available. This condition has led to what is generally referred to as the "blunt body problem." Some gains have been made in recent years toward the solution of this problem by various numerical and approximate methods – for example, see references 1 to 6; however, as discussed in reference 7, large discrepancies can exist between the pressure distributions determined by the different methods. Until the problems associated with these discrepancies are resolved, experimental investigations are required to determine the local flow properties on all but the more basic nose shapes.

A blunt nose shape that has received considerable attention in the past and that has been used on numerous reentry configurations (e.g., Mercury, Gemini, and Apollo) consists of a hemispherical segment nose with a shoulder region having a circular cross section. Experimentally obtained stagnation-point velocity gradients for bodies of this type with a shoulder radius of zero have been reported in reference 8 and with a limited range of shoulder radius, in reference 9. Although the stagnation-point velocity gradients are extremely important for determining the stagnation-point heating, it is well known that for extremely blunt bodies the maximum heating occurs off the stagnation point. Therefore, in order to assess accurately the level of heating over such a family of bodies, detailed pressure and velocity distributions must be determined over the complete nose. Pressure distributions for such bodies have been reported in references 8, 10, and 11; however, the models used in these investigations provided only a limited range of geometrical variables and, being small, were limited in the amount of instrumentation.

The present investigation was therefore initiated to determine the effect of nose and shoulder radii on the local pressure and velocity distributions for a family of 18 blunt bodies. The models, which were 7.5 inches (191 mm) in diameter, ranged from a hemispherical nose to a flat-face cylinder at intervals of nose and shoulder radii sufficiently small to enable the results from this investigation to be applied – either directly or by interpolation – to any shape of the general type. The tests were conducted through a range of Mach number from 2.49 to 4.63. The flow properties presented and discussed for the complete range of geometrical variables consist of pressure distributions, velocity distributions, stagnation-point velocity gradients, and shock-standoff distances. Drag coefficients obtained by integrating the local pressures are also discussed. Limited comparisons are made with approximate theories.

SYMBOLS

a^*	free-stream sonic velocity
A	area
C_D	drag coefficient
C_p	pressure coefficient
$C_{p,max}$	maximum pressure coefficient, based on total pressure behind normal shock
D	drag force
d	afterbody diameter
M	Mach number
p	pressure
r_b	afterbody radius
r_c	shoulder (corner) radius
r_n	nose radius
s	surface length, measured from forward stagnation point (see fig. 1)
s_1	nose surface length from forward stagnation point to point of tangency of nose and shoulder arcs (see fig. 1)
s_2	nose surface length from forward stagnation point to shoulder-afterbody juncture (see fig. 1)
T	temperature
u	velocity
u'	stagnation-point velocity gradient, du/ds
θ	angle between normal to model surface and axis of symmetry (see fig. 1)
θ_1	value of θ at s_1
γ	ratio of specific heats, 1.4 for air

δ	shock-standoff distance
ρ	density

Subscripts:

∞	free-stream conditions
l	local static conditions at outer edge of boundary layer
t	free-stream stagnation conditions
t,2	stagnation conditions behind normal shock at free-stream Mach number
b	pertaining to model base
h	pertaining to hemisphere

APPARATUS AND TEST CONDITIONS

The investigation was conducted in the high Mach number test section of the Langley Unitary Plan wind tunnel described in reference 12. This variable-pressure, continuous flow tunnel has an asymmetric sliding-block nozzle that permits a continuous variation in the test-section Mach number from 2.30 to 4.63. The deviations in Mach number in the entire 4- by 4-foot (1.22- by 1.22-meter) test section for the test Mach numbers are as follows:

For $M_\infty = 2.49$	± 0.018
For $M_\infty = 3.51$	± 0.048
For $M_\infty = 4.06$	± 0.061
For $M_\infty = 4.63$	± 0.045

The effects of nonuniform Mach number were minimized in this investigation by testing all models at essentially the same location in the test section. The effect of flow angularity associated with this nonuniform Mach number was also minimized by an adjustment of the models for each test point relative to the free-stream velocity vector. This step was accomplished by monitoring pressure differentials from the stagnation point to orifice locations equidistant and diametrically opposite the stagnation point and adjusting the model in both angle of attack and angle of yaw until these pressure differences equalized.

The pressure measurements were obtained for the model at an angle of attack of 0°. The free-stream stagnation temperatures at the test Mach numbers were as follows:

M_∞	T_t, $^{\circ}R$	T_t, $^{\circ}K$
2.49	610	339
3.51	610	339
4.06	635	353
4.63	635	353

The test Reynolds number, based on afterbody diameter, was 1.88×10^6.

MODELS, INSTRUMENTATION, AND ACCURACY

The general shape of the axisymmetrical models (see fig. 1) consisted of a hemispherical segment nose (of radius r_n) faired into a circular-arc shoulder (of radius r_c) which faired into a cylindrical afterbody (of diameter d). A total of 18 models were tested and they had geometries ranging from a flat-face cylinder $\left(\frac{r_c}{d} = 0, \frac{r_n}{d} = \infty\right)$ to a hemisphere $\left(\frac{r_c}{d} = 0.5, \frac{r_n}{d} = 0.5\right)$. Values of r_c/d and r_n/d for each model are shown in the table presented in figure 1. Also included in this table are values of s_1/d and s_2/d, where s_1 is the value of s at the point of tangency of the nose and shoulder arcs and s_2 is the value of s at the shoulder-afterbody juncture. The afterbody for all models consisted of a cylindrical section 4 inches (102 mm) long and 7.5 inches (191 mm) in diameter. The model instrumentation consisted of approximately 80 pressure orifices of 0.050-inch (1.27-mm) inside diameter. Locations of these pressure orifices for a typical model are shown on the sketch in figure 1. Photographs of each model tested are shown in figure 2, and a typical model installation in the test section is shown in figure 3.

In the forward stagnation region of blunt bodies, the pressure magnitudes are generally quite large; however, the pressure gradients can be very small. Such a combination makes it extremely difficult, if not impossible, to measure the magnitude of the pressure decrease with surface length within this region with an absolute-pressure gage to the precision required for accurately determining local velocity gradients. This problem was minimized in this investigation by using a sensitive differential-pressure gage, full-scale deflection of 1 psi (6895 N/m^2), to measure the pressure differential from the forward stagnation point to a select number of locations. The magnitudes of the pressures at

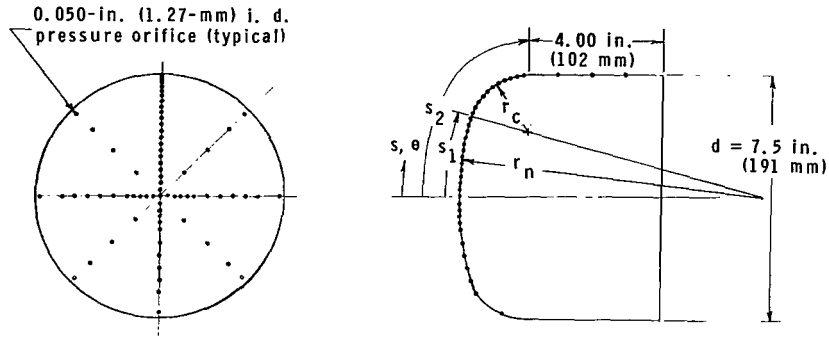

Model shape	Model	$\frac{r_n}{d}$	$\frac{r_c}{d}$	$\frac{s_1}{d}$	$\frac{s_2}{d}$	Model shape	Model	$\frac{r_n}{d}$	$\frac{r_c}{d}$	$\frac{s_1}{d}$	$\frac{s_2}{d}$
	1	∞	0	0.500	0.500		10	1.933	0.400	0.126	0.728
	2		0.100	0.400	0.557		11	1.000	0	0.524	0.524
	3		0.200	0.300	0.614		12		0.200	0.384	0.622
	4		0.300	0.200	0.672		13		0.300	0.290	0.674
	5		0.400	0.100	0.728		14		0.400	0.167	0.729
	6	1.933	0	0.506	0.506		15	0.707	0	0.555	0.555
	7		0.100	0.425	0.560		16		0.200	0.448	0.635
	8		0.200	0.336	0.616		17	0.577	0	0.605	0.605
	9		0.300	0.237	0.672		18	0.500 to ∞ 0.500	0.500 0	0.785	0.785

Figure 1.- Model geometry.

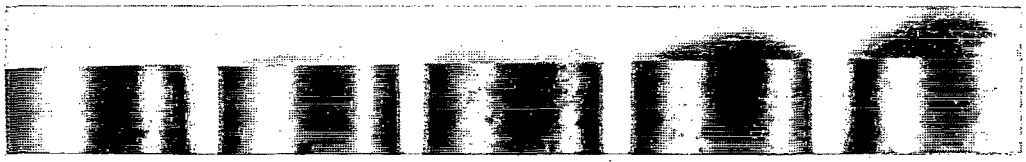

$r_n/d = \infty$ Model 1 | $r_n/d = 1.933$ Model 6 | $r_n/d = 1.000$ Model 11 | $r_n/d = 0.707$ Model 15 | $r_n/d = 0.577$ Model 17

(a) $r_c/d = 0$.

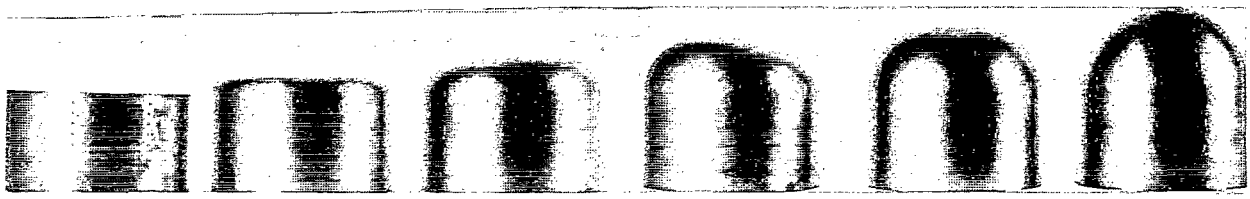

$r_c/d = 0$ Model 1 | $r_c/d = 0.100$ Model 2 | $r_c/d = 0.200$ Model 3 | $r_c/d = 0.300$ Model 4 | $r_c/d = 0.400$ Model 5 | $r_c/d = 0.500$ Model 18

(b) $r_n/d = \infty$.

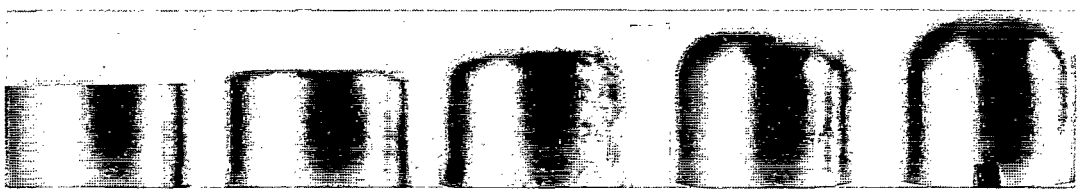

$r_c/d = 0$ Model 6 | $r_c/d = 0.100$ Model 7 | $r_c/d = 0.200$ Model 8 | $r_c/d = 0.300$ Model 9 | $r_c/d = 0.400$ Model 10

(c) $r_n/d = 1.933$.

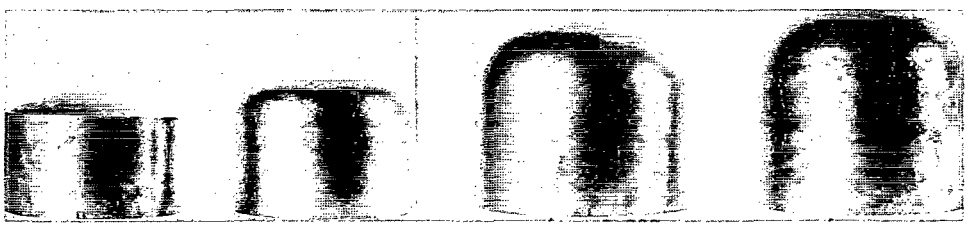

$r_c/d = 0$ Model 11 | $r_c/d = 0.200$ Model 12 | $r_c/d = 0.300$ Model 13 | $r_c/d = 0.400$ Model 14

(d) $r_n/d = 1.000$.

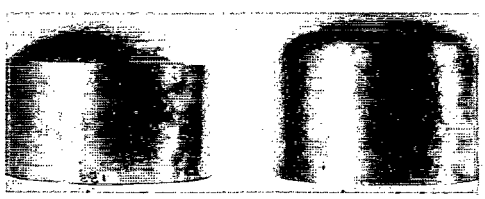

$r_c/d = 0$ Model 15 | $r_c/d = 0.200$ Model 16

(e) $r_n/d = 0.707$.

Figure 2.- Model photographs. L-67-1073

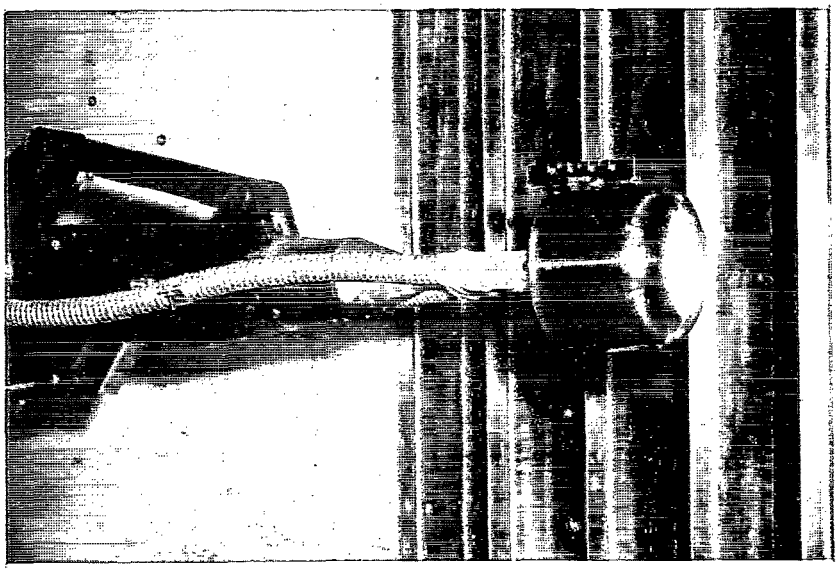

Figure 3.- Typical model installation in test section. L-65-7350

these locations were obtained by subtracting the pressure differentials from the stagnation-point pressure which was measured with a precision mercury manometer. The pressures at all remaining locations were measured with an absolute transducer having a full-scale deflection of 10 psi (68 950 N/m^2). Both the 1- and 10-psi (6895- and 68 950-N/m^2) transducers were used in conjunction with a multichannel scanning system so that only a total of four transducers were required. The output from each electrical transducer was recorded with a digital self-balancing potentiometer.

The tunnel free-stream static and total pressures were measured with precision mercury manometers. The accuracy of the precision mercury manometers is within 0.5 psf (23.94 N/m^2); therefore, the accuracy of the pressure measuring system is limited to that of the electrical transducers. The accuracy of the electrical transducers is within 1 percent of full-scale deflection, which corresponds to a pressure increment of 1.44 and 14.4 psf (69 and 690 N/m^2) for the 1- and 10-psi (6895- and 68 950-N/m^2) gages, respectively.

RESULTS AND DISCUSSION

Pressure Distributions

The effect of Mach number on the hemisphere pressure distributions is shown in figure 4 for the test range of Mach number from 2.49 to 4.63. The local measured pressures have been normalized by the measured pressure at $s/d = 0$. The effect of Mach number, as expected, consists of a decrease in the magnitude of the normalized pressure

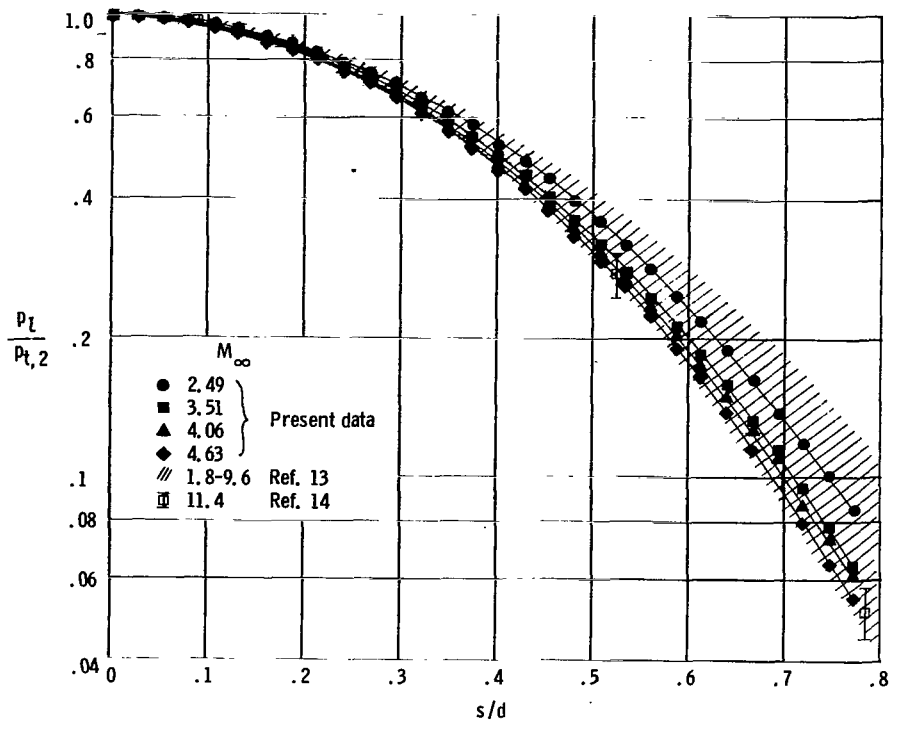

Figure 4.- Comparison of pressure distributions obtained on hemispherical model with previously published results.

distributions; the extent of this effect decreased with increasing Mach number. Also shown in this figure are experimental data from references 13 and 14 for Mach numbers up to 11.4. The data obtained from reference 13, indicated by the hatched region, cover a range of Mach number from 1.8 to 9.6. The Mach number 1.8 data are at the upper bound of the hatched region and the $M = 9.6$ data are near or at the lower bound of this region. There is only a very slight difference between the $M = 4.63$ data of the present tests and the higher Mach number data of both references 13 and 14.

Presented in figure 5 is the effect of nose radius on the normalized pressure distributions for the zero-corner-radius models. The two extreme geometries are the flat-face cylinder $\left(\frac{r_n}{d} = \infty\right)$ and the hemisphere $\left(\frac{r_n}{d} = 0.500\right)$. The dashed parts of the curves for $\frac{r_n}{d} = 1.000$, 1.933, and ∞ are extrapolations from the pressure measurements on these models at the last instrumentation station to the pressure corresponding to sonic velocity, which for these models would occur at $s = s_2$. For the other three models, the sonic point location occurred at $s < s_2$.

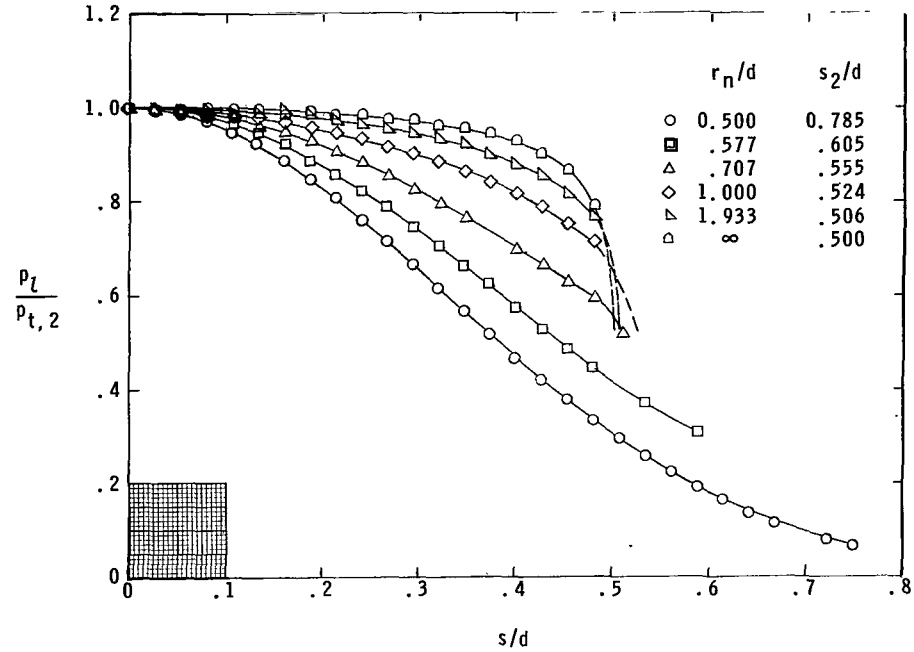

Figure 5.- Effect of nose radius on pressure distributions of zero-corner-radius models. $M_\infty = 4.63$.

The effect of shoulder radius on the pressure distributions for constant values of r_n/d is shown in figure 6. The test-point symbol notation corresponds to the same values of r_c/d for all parts of figure 6; however, the values of s_2/d are a function of r_n/d and therefore may have different values for the same symbol. The short-dashed curves for $\frac{r_c}{d} = 0$ in figures 6(a), 6(b), and 6(c) are the same extrapolations shown in figure 5. The long-dashed curves labeled s_1/d represent the location on the pressure-distribution curves of the point of tangency of the nose and shoulder arcs for each model. The data represented by the circular symbols $\left(\frac{r_c}{d} = 0.5\right)$ were obtained on the hemispherical model and are therefore independent of r_n/d. The curve for $\frac{r_c}{d} = 0.5$ also represents one of the limiting cases for each value of r_n/d. The other limiting case is the pressure distributions for the zero-corner-radius models, which are a function of r_n/d. With decreasing values of r_n/d, these distributions approach the distribution for the hemispherical model which reduces the extent of the corner-radius effect.

A modified Newtonian pressure distribution was evaluated from the following expression for $\frac{r_c}{d} = 0$:

$$\frac{p_l}{p_{t,2}} = \cos^2\left(\frac{s}{d}\frac{d}{r_n}\right) + \frac{p_\infty}{p_{t,2}}\sin^2\left(\frac{s}{d}\frac{d}{r_n}\right) \qquad (1)$$

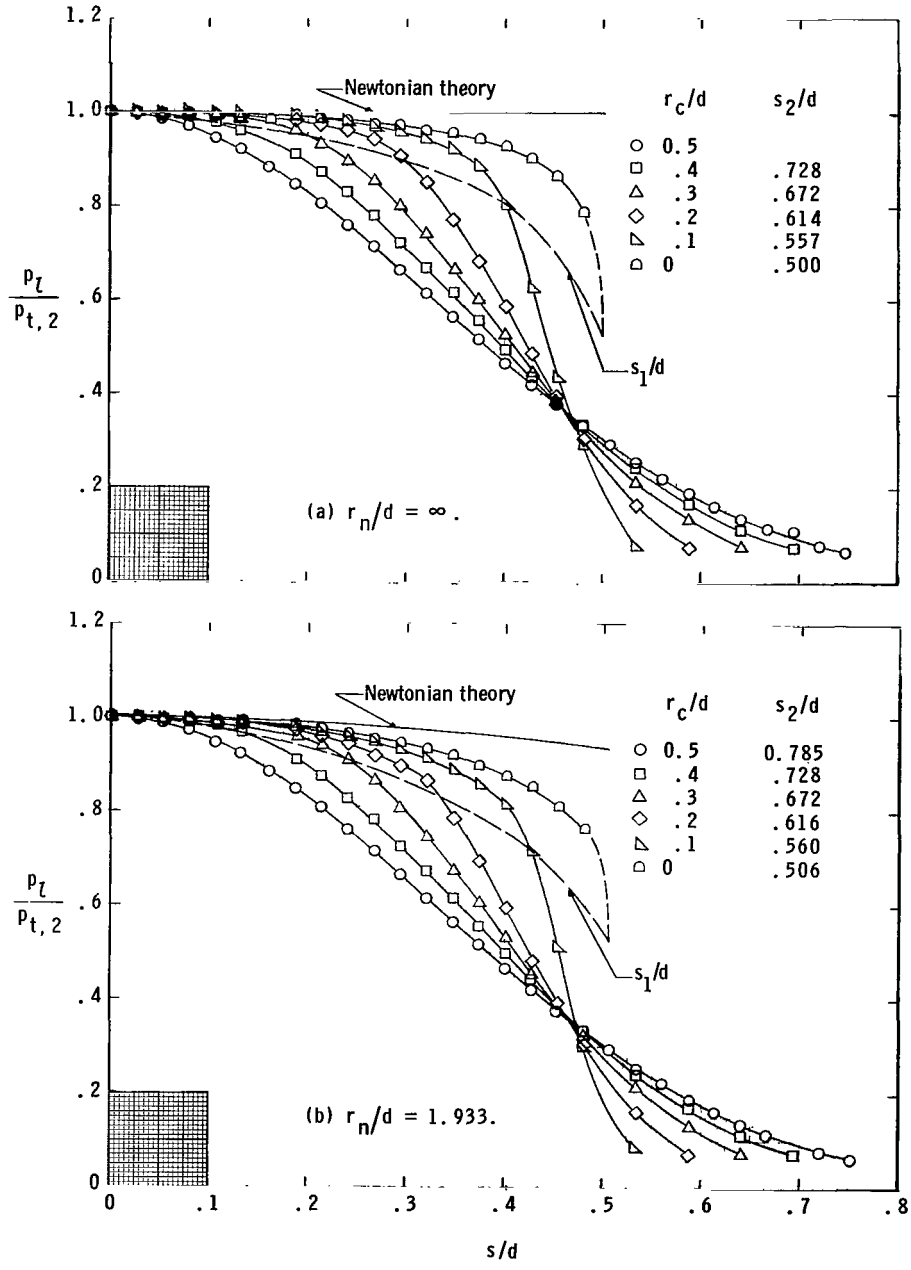

Figure 6.- Effect of shoulder radius on pressure distributions. $M_\infty = 4.63$.

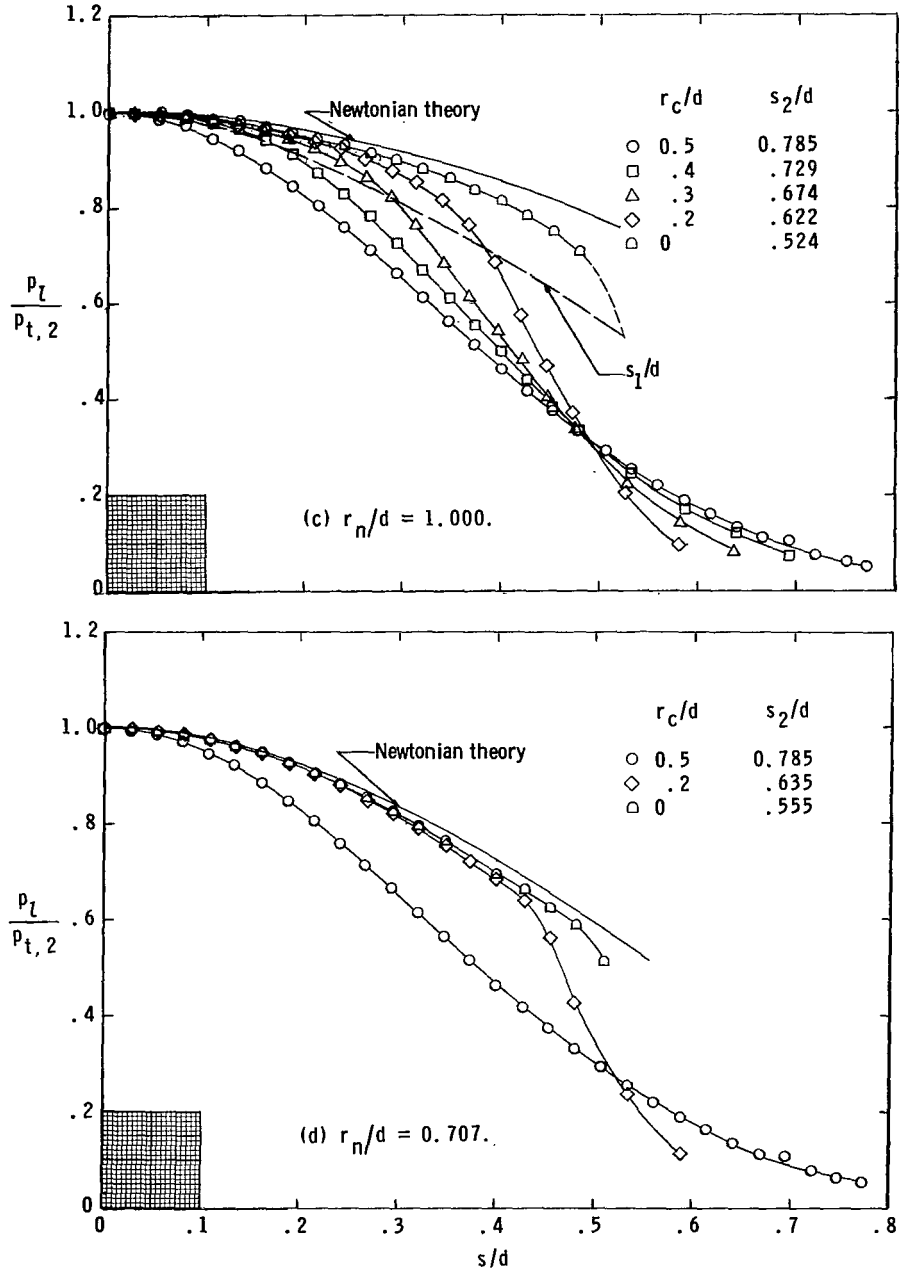

Figure 6.- Concluded.

and is presented for each value of r_n/d in figure 6. This theoretical distribution should also apply to those models having $\frac{r_c}{d} > 0$ where $\frac{s}{d} < \frac{s_1}{d}$ since within this range of s/d the local surface slopes are the same. The limitation of the Newtonian theory for predicting either the pressure magnitudes or the pressure distributions for $1.0 \leqq \frac{r_n}{d} \leqq \infty$ when $\frac{r_c}{d} < 0.5$ is clearly indicated in figures 6(a), 6(b), and 6(c). As expected, for those models having $\frac{r_n}{d} = 0.707$ (fig. 6(d)), much better agreement is shown with the Newtonian theory because the local surface slope at the shoulder juncture for these models is approximately the same as that at the sonic point for the hemispherical model. It is interesting to note that for each value of r_n/d the pressure-distribution curves intersect each other at a common location (other than at the stagnation point) for values of $0.2 \leqq \frac{r_c}{d} \leqq 0.5$. The value of s/d at which this intersection occurs appears to increase slightly with decreasing values of r_n/d.

The effect of decreasing Mach number from 4.63 to 2.49 on the normalized pressure distributions is shown in figure 7 for selected values of r_c/d at each value of r_n/d. A

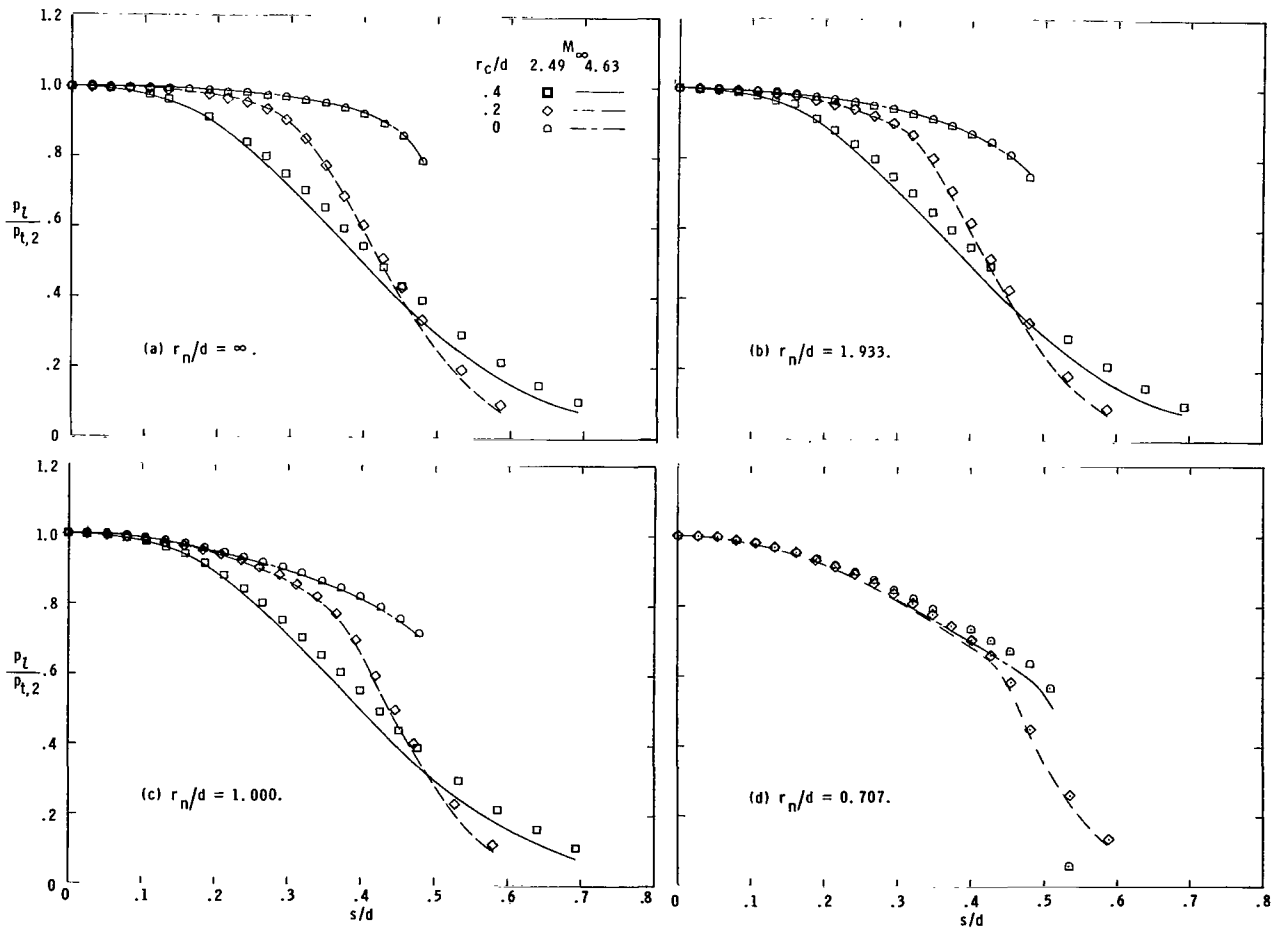

Figure 7.- Effect of Mach number on pressure distributions.

comparison of these distributions, together with the Mach number effect shown for the hemispherical model in figure 4, clearly indicates that the Mach number effect rapidly diminishes with increasing nose bluntness (with decreasing shoulder radius). Furthermore, since the results for the hemispherical model at $M_\infty = 4.63$ were in good agreement with higher Mach number results (from refs. 13 and 14), the data included in this paper for all models should be applicable at much higher Mach numbers so long as real-gas effects can be neglected.

Drag Coefficients

Drag coefficients were determined for each model through the test range of Mach number from integrated pressure measurements. Since the base of the models was not instrumented, the drag increment resulting from base pressure was estimated from the following often-used empirical expression:

$$C_{D,b} = C_{p,b} = -\frac{1}{M_\infty^2} \tag{2}$$

With this relationship being assumed for $C_{D,b}$, a comparison of C_D for the hemispherical model with existing experimental flight data for a sphere is shown in figure 8. Good agreement is shown between the present data and previously published data (refs. 15 to 18). Also shown are the drag coefficients calculated for a base pressure equal to free-stream static pressure, as implied by Newtonian theory. These drag coefficients (solid circular test points) are considerably lower than the flight data at the lower test Mach

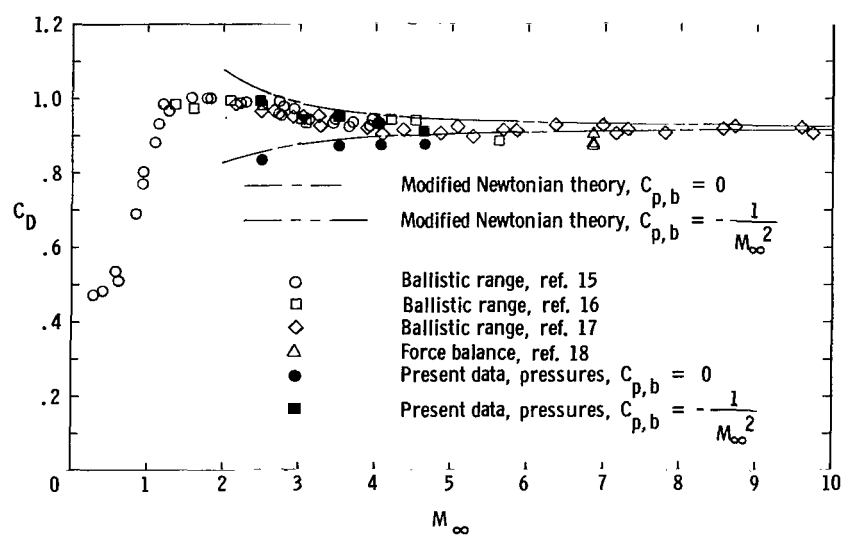

Figure 8.- Variation with Mach number of drag coefficients for hemispherical model.

numbers although the magnitude of the disagreement decreases with increasing Mach number. The drag coefficients evaluated from the modified Newtonian theory

$$C_D = \frac{C_{p,max}}{2} - C_{p,b} \tag{3}$$

are based on the standard Newtonian assumption $C_{p,b} = 0$ as well as on the expression $C_{p,b} = -\frac{1}{M_\infty{}^2}$. Use of the $-1/M_\infty{}^2$ relation for $C_{p,b}$, as shown in figure 8, gives much better agreement between experiment and theory at the lower Mach numbers. At the higher Mach numbers, the values of $C_{p,b} = -\frac{1}{M_\infty{}^2}$ approach zero and therefore the drag coefficients approach the standard Newtonian values.

The effects of shoulder and nose radii on the drag coefficients for all test Mach numbers are presented in figure 9. The effect of shoulder radius for a given nose radius can be seen by observing the variation of a given test-point symbol with r_c/d whereas the effect of nose radius is shown by the different symbols at a constant shoulder radius.

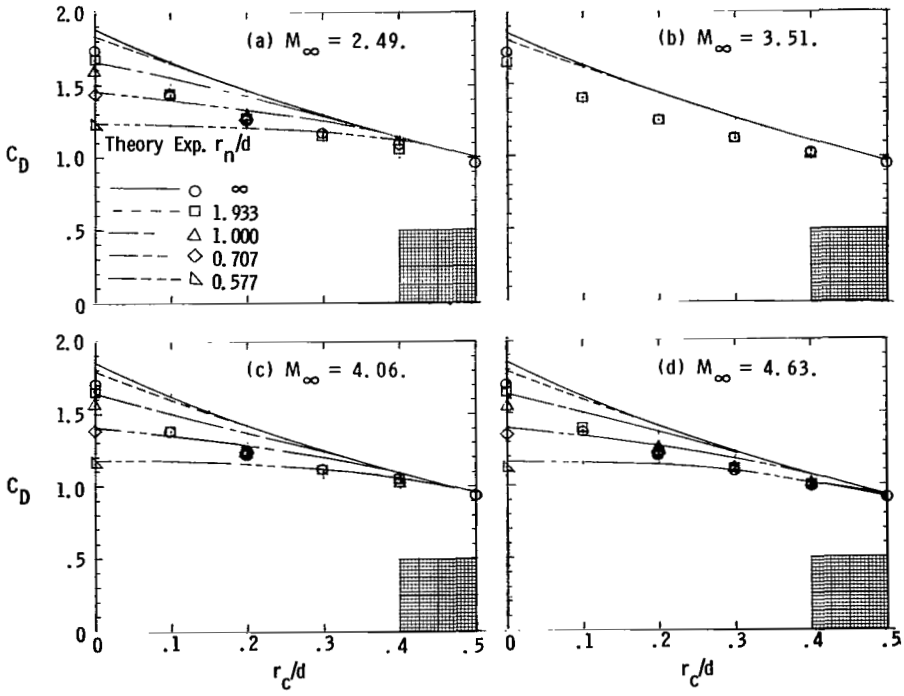

Figure 9.- Variation of drag coefficients with model nose geometry.

Theoretical values, determined from modified Newtonian theory, were evaluated from the following equations as derived in appendix A:

For $\frac{r_n}{r_b} < \infty$,

$$C_D = \frac{1}{2}\left(\frac{r_n}{r_b}\right)^2 C_{p,max}\left(1 - \cos^4\theta_1\right) + 2C_{p,max}\frac{r_c}{r_b}\left(1 - \frac{r_c}{r_b}\right)\left[\frac{2}{3} - \frac{1}{3}\sin\theta_1\left(\cos^2\theta_1 + 2\right)\right]$$

$$+ \frac{1}{2} C_{p,max}\left(\frac{r_c}{r_b}\right)^2 \cos^4\theta_1 + \frac{1}{M_\infty{}^2} \tag{4}$$

and for $\frac{r_n}{r_b} = \infty$,

$$C_D = C_{p,max}\left(1 - \frac{r_c}{r_b}\right)^2 + \frac{4}{3} C_{p,max}\frac{r_c}{r_b}\left(1 - \frac{r_c}{r_b}\right) + \frac{1}{2} C_{p,max}\left(\frac{r_c}{r_b}\right)^2 + \frac{1}{M_\infty{}^2} \tag{5}$$

For $M_\infty = 2.49$ (fig. 9(a)), the drag coefficients decrease with either decreasing nose radius or increasing shoulder radius because of a reduction in the extent of bluntness; however, the effect of nose radius decreases with an increase in shoulder radius. Although this trend is shown by both experiment and theory, the decrease in the effect of nose radius on C_D with an increase in shoulder radius occurs much more rapidly for the experimental data. In fact, for $\frac{r_c}{d} = 0.2$, the experimentally obtained drag coefficients remained essentially constant for $0.707 \leqq \frac{r_n}{d} \leqq \infty$ whereas the theoretical drag coefficients decrease by approximately 9 percent as a result of this range of reduction in r_n/d.

For the flat-face cylinder model $\left(\frac{r_n}{d} = \infty, \ \frac{r_c}{d} = 0\right)$, the experimental drag coefficient is less than the theoretical Newtonian value by approximately 8 percent. This disagreement results from the fact that the physical flow expands to sonic velocity at the shoulder with the corresponding reduction in local pressure (see fig. 6(a)) whereas the Newtonian theory predicts a constant pressure across the face. For $\frac{r_c}{d} = 0$, the agreement between theory and experiment improves with decreasing r_n/d so that for $\frac{r_n}{d} \leqq 0.707$ the disagreement is within the data accuracy. Intuitively, the agreement between theory and experiment would be expected to improve with increasing values of r_c/d at a constant value of r_n/d since the body geometry approaches the hemispherical shape for which the Newtonian theory is known to give good results. As shown in figure 9(a), this improvement occurs for values of $\frac{r_c}{d} > 0.2$; however, for values of $\frac{r_c}{d} < 0.2$, the theoretical and experimental curves diverge with increasing r_c/d for $0.707 \leqq \frac{r_n}{d} \leqq \infty$. The maximum disagreement is approximately 16 percent and occurred for $\frac{r_n}{d} = \infty$ and $\frac{r_c}{d} = 0.1$ or 0.2.

The same general trends in the variation of drag coefficient with model geometry as shown for $M = 2.49$ are shown in figures 9(b), 9(c), and 9(d) for Mach numbers 3.51, 4.06, and 4.63, respectively. The results presented in figure 9(d) are replotted in figure 10 in order to show more clearly the effect of nose radius on the drag coefficients. Note that the abscissa scale in figure 10 is the inverse of the parameter r_n/d used in the key of figure 9. This change was made in order to eliminate the broken scale that would be required to show the results obtained at $\frac{r_n}{d} = \infty$. As previously discussed, the variation of C_D with r_n/d is very small for $\frac{r_c}{d} = 0.2$; however, these data, as presented in figure 10, actually indicate a slight increase in C_D with increasing d/r_n for $\frac{d}{r_n} \leq 1.0$. This trend, which is contrary to what might be expected (since increasing d/r_n decreases the extent of bluntness), is also indicated for values of $\frac{r_c}{d} = 0.1$ and 0.3.

Velocity Distributions

Velocity distributions for the hemispherical model, nondimensionalized by sonic velocity, are presented in figure 11 for the test Mach number range. Also shown in this figure are distributions obtained by previous investigators (refs. 13 and 14 and 19 to 22) for Mach numbers from 1.97 to 11.4. The referenced data for Mach numbers from 1.97 to 6.8 as shown by the faired curves are in good agreement with the present results for both the

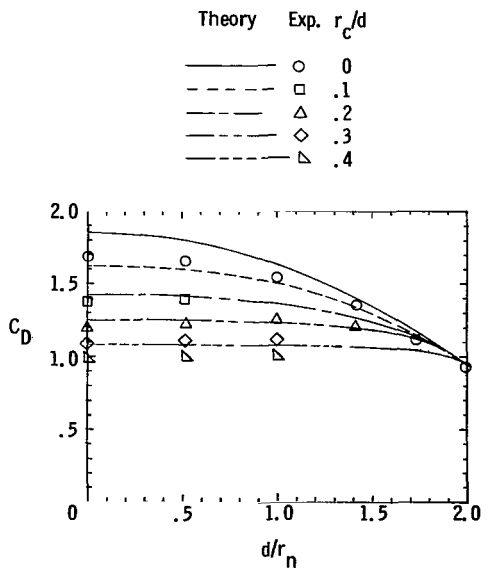

Figure 10.- Effect of nose radius on drag coefficients. $M_\infty = 4.63$.

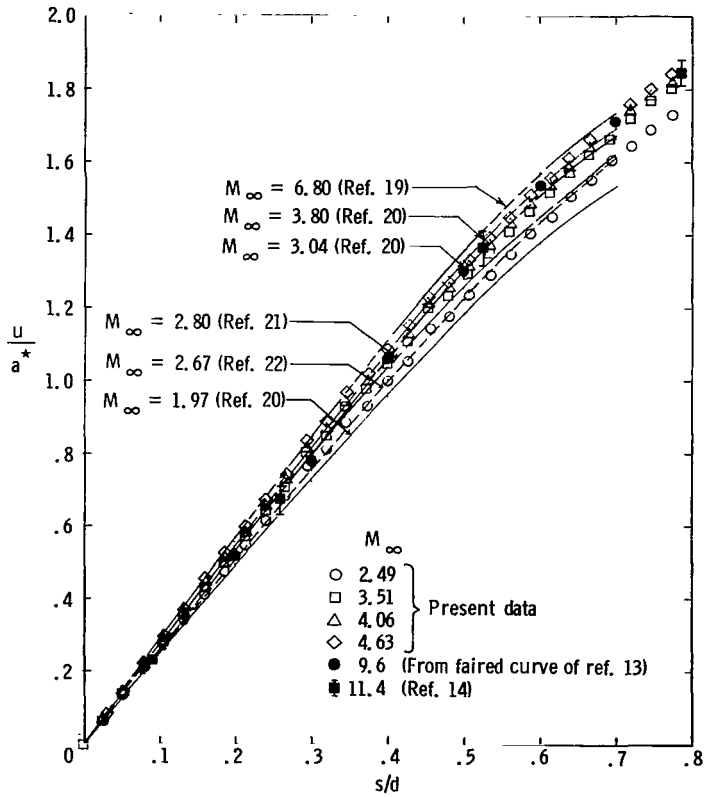

Figure 11.- Effect of Mach number on velocity distributions for hemispherical model.

velocity distributions and the magnitude of the Mach number effect on these distributions. The velocity distributions shown for $M_\infty = 9.6$ (ref. 13) and $M_\infty = 11.4$ (ref. 14) are slightly less than those shown for either $M_\infty = 6.8$ (ref. 19) or $M_\infty = 4.63$ of the present tests. This apparent discrepancy of approximately 5 percent is probably within the accuracy of the referenced results for the higher Mach number.

The nondimensional velocity distributions obtained on the zero-corner-radius models are shown in figure 12 for $M_\infty = 4.63$. The test-point symbols in this figure correspond to the same geometrical variables used for the pressure results presented in figure 5. In order to improve the accuracy of the velocity distributions for small values of s/d, these as well as all subsequent velocity distributions were determined from averaged pressures around the face of the models. This averaging process could result in slight differences for velocities computed from the pressures presented in figure 5 which are only for one instrumented ray. For all values checked, the deviation of the averaged velocity from those along any particular ray was well within the instrumentation accuracy.

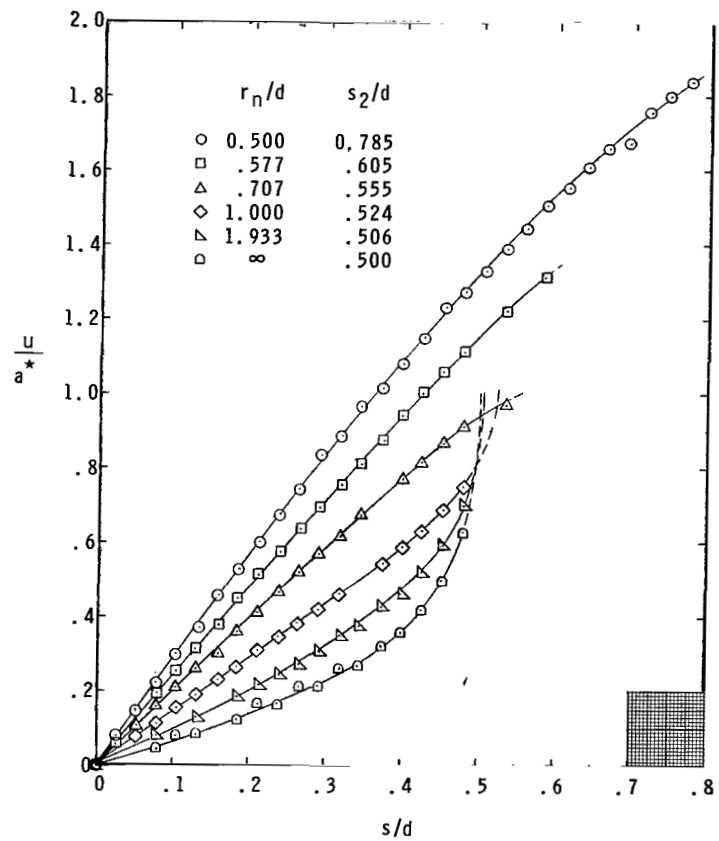

Figure 12.- Effect of nose radius on velocity distributions of zero-corner-radius models. $M_\infty = 4.63$.

The effect of shoulder radius on the nondimensional velocity distributions for constant values of r_n/d is presented in figure 13. The dashed curves labeled s_1/d again represent the location of the point of tangency of the nose and shoulder arcs for each value of r_c/d as shown previously in the figures of pressure data. Although no apparent unique characteristic of the pressure-distribution curves occurred at s_1/d, an inflection occurred in the velocity-distribution curves either at or slightly downstream of this location for $\frac{r_c}{d} > 0$ and all values of r_n/d. This inflection corresponds to the maximum velocity gradient, the magnitude of which decreases with increasing r_c/d at constant values of r_n/d. As the values of r_n/d are increased, the velocity-distribution curves for the two limiting models $\left(\text{with shoulder radii } \frac{r_c}{d} = 0 \text{ and } 0.5\right)$ tend to move toward each other and therefore reduce the overall effect of r_c/d. This tendency is similar to that shown by the results for the pressure distributions.

The effect of Mach number on the nondimensional velocity distributions is shown in figure 14 for selected geometrical shapes, as well as in figure 11 for the limiting hemispherical model. The extent of the Mach number effect decreases with increasing bluntness similar to that shown by the pressure-distribution results. The velocity-distribution results for the zero-corner-radius models with $\frac{r_n}{d} > 0.707$ show no Mach

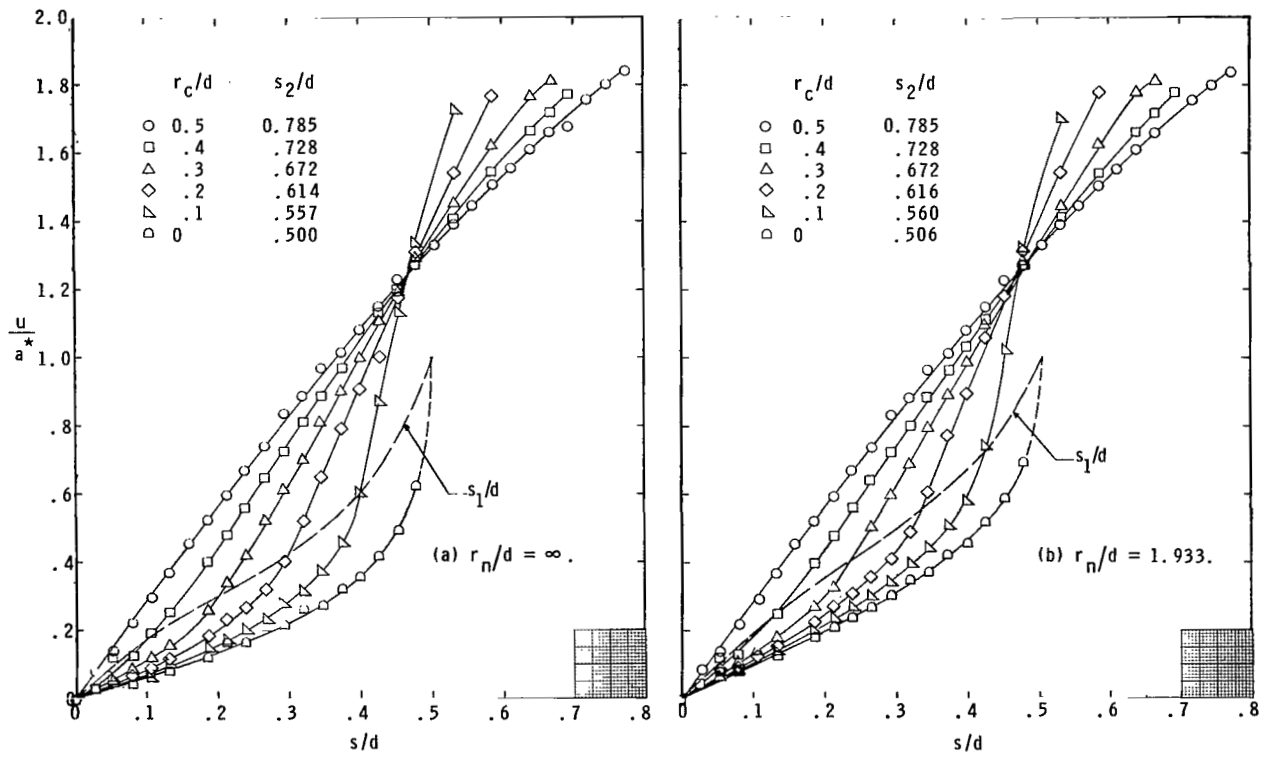

Figure 13.- Effect of shoulder radius on velocity distributions for constant nose radius. $M_\infty = 4.63$.

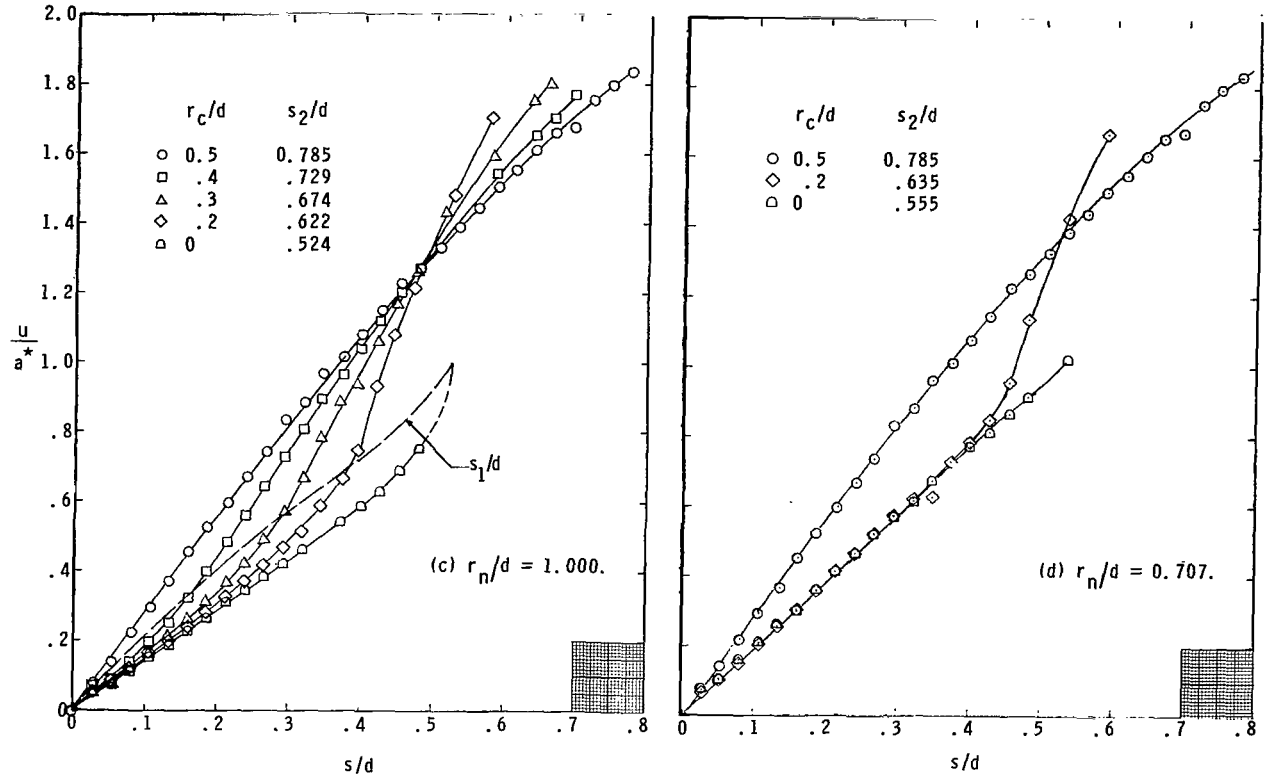

Figure 13.- Concluded.

number effect whereas those for the models with $\frac{r_n}{d} = 0.707$ show an increase with increasing Mach number. This increase is due to the fact that the sonic point for $\frac{r_n}{d} > 0.707$ is fixed at the shoulder, whereas the sonic point for $\frac{r_n}{d} = 0.707$ has moved forward of this juncture so that the Mach number effect is essentially the same as for a hemisphere.

Stagnation-Point Velocity Gradients

Stagnation-point velocity gradients were determined graphically from large-scale plots of the averaged velocity measurements in the stagnation region of the models. Only those velocities evaluated from the pressures measured with the 1-psi (6895-N/m^2) transducers were used. Typical velocity distributions and the linear fairings for the stagnation region are shown in figure 15.

A correlation parameter derived from modified Newtonian theory and the incompressible Bernoulli equation was used to correlate the stagnation-point velocity gradients for the hemispherical model with those obtained from references 19, 20, and 22 to 24.

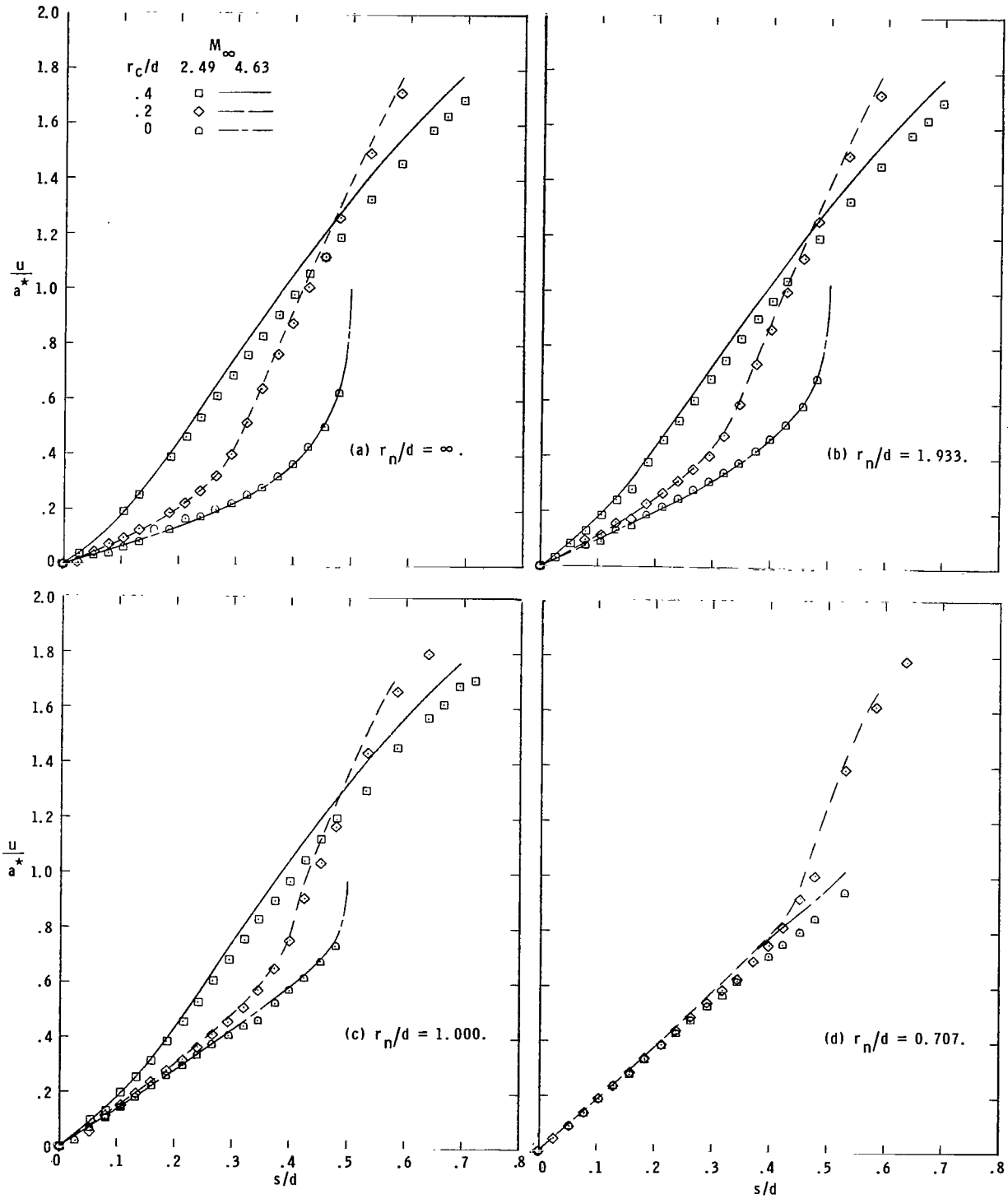

Figure 14.- Effect of Mach number on velocity distributions.

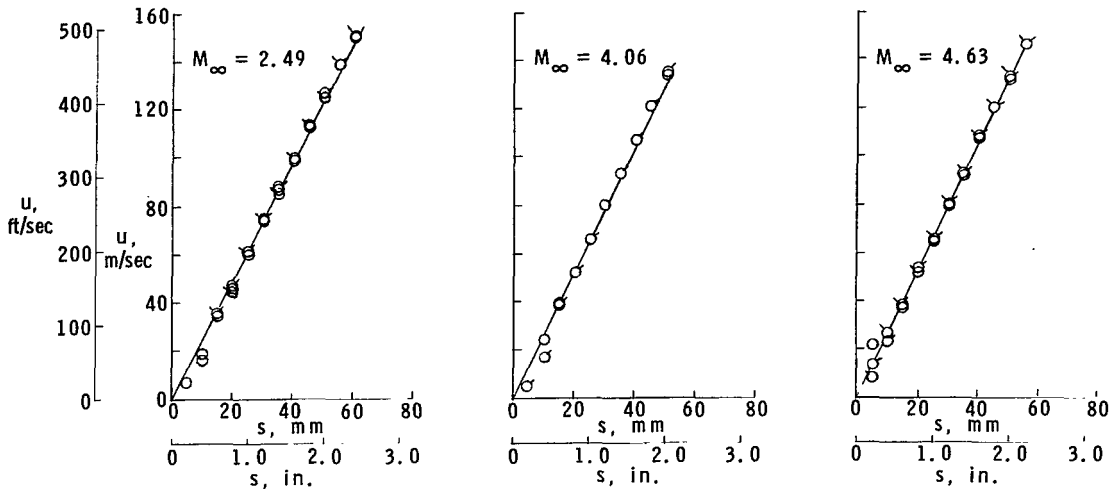

(a) Model 11; $r_c/d = 0$; $r_n/d = 1.000$.

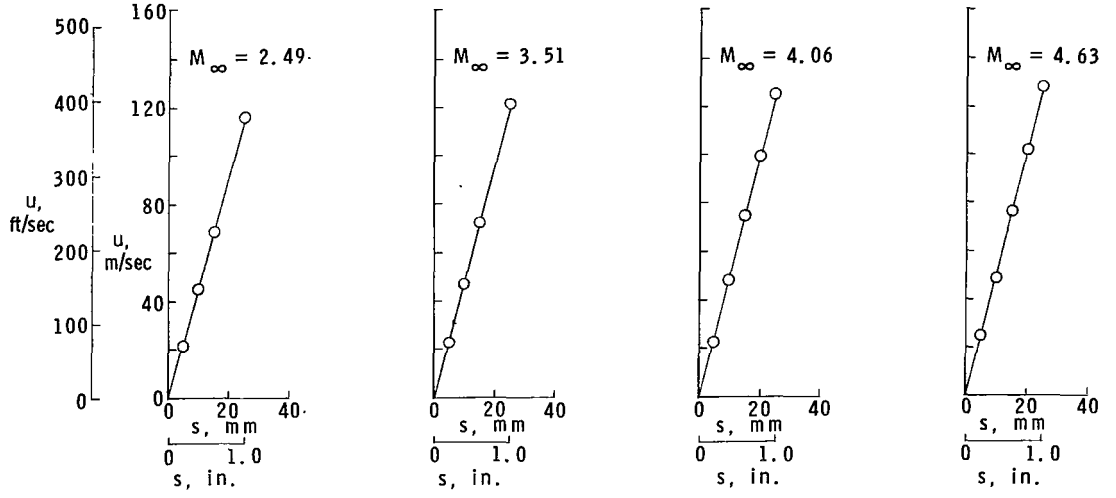

(b) Model 18; $r_c/d = 0.500$; $r_n/d = 0.500$.

Figure 15.- Typical velocity distributions in stagnation region of models.

From the modified Newtonian theory, the pressure distribution can be expressed as

$$\frac{p_l}{p_{t,2}} = \cos^2\theta + \frac{p_\infty}{p_{t,2}} \sin^2\theta \tag{6}$$

and from the incompressible Bernoulli equation, which is valid within the model stagnation region, the velocities can be written in terms of pressures as follows:

$$u = \left[\frac{2p_{t,2}}{\rho_{t,2}}\left(1 - \frac{p_l}{p_{t,2}}\right)\right]^{1/2} \tag{7}$$

Combining equations (6) and (7) and simplifying yields

$$u = \sin\theta\left[\frac{2p_{t,2}}{\rho_{t,2}}\left(1 - \frac{p_\infty}{p_{t,2}}\right)\right]^{1/2} \tag{8}$$

Since for small values of θ,

$$\sin\theta \approx \theta$$

the following expression is obtained:

$$u \approx \theta\left[\frac{2p_{t,2}}{\rho_{t,2}}\left(1 - \frac{p_\infty}{p_{t,2}}\right)\right]^{1/2} \tag{9}$$

Differentiating equation (9) with respect to s, where

$$u' = \frac{du}{d\theta}\frac{d\theta}{ds} = \frac{1}{r_n}\frac{du}{d\theta}$$

the stagnation-point velocity gradient for air can be expressed as

$$\frac{r_n u'}{\left[T_t\left(1 - \frac{p_\infty}{p_{t,2}}\right)\right]^{1/2}} \approx 58.6 \tag{10}$$

The parameter on the left-hand side of equation (10) was evaluated for the stagnation-point velocity gradients obtained on the hemispherical model and is presented in figure 16 as a function of Mach number. Also shown in figure 16 are results obtained from references 19, 20, and 22 to 24 for Mach numbers up to 6.8. The results from the present investigation fall within the data scatter of the previously obtained results and all results are within ±7 percent of the constant value predicted by equation (10).

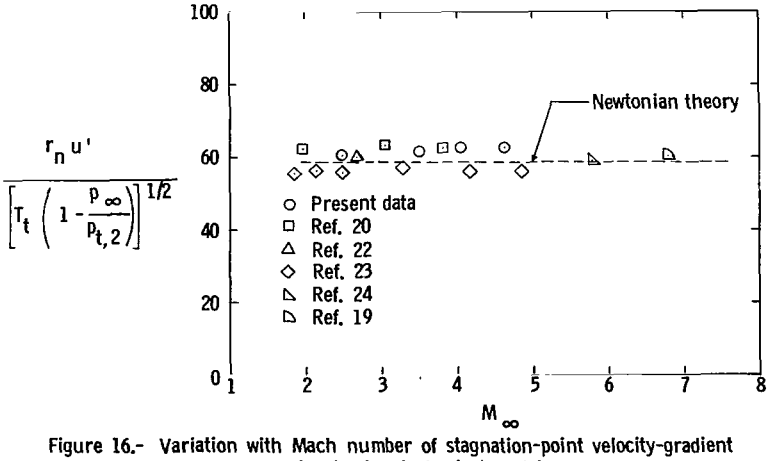

Figure 16.- Variation with Mach number of stagnation-point velocity-gradient parameter for hemispherical model.

Since Newtonian theory has limited application to the other models of this investigation, the use of equation (10) was restricted to the hemisphere. In an attempt to minimize the Mach number effect on stagnation-point velocity gradients for the other models, the velocity gradients were nondimensionalized by the values obtained from the hemispherical model at each test Mach number. This parameter was used inasmuch as the stagnation-point velocity gradients for all models decreased monotonically with increasing Mach number. These nondimensional velocity gradients are presented in figure 17 for all models investigated through the test range of Mach number. Also shown in figure 17 are data obtained from reference 8 for values of $\frac{r_c}{d} = 0$ and $\frac{r_n}{d} = \infty$ and 1.0. These results are approximately 6 percent greater than those of the present tests. The values of u'_h used for nondimensionalizing the reference 8 data were determined from modified Newtonian theory. However, as shown in figure 16, the measured values of u' for the hemispherical model for the present tests are approximately 7 percent greater than those obtained by the Newtonian theory and this discrepancy is believed to be the major source of the difference between the two sets of u/u'_h data. The theoretical values

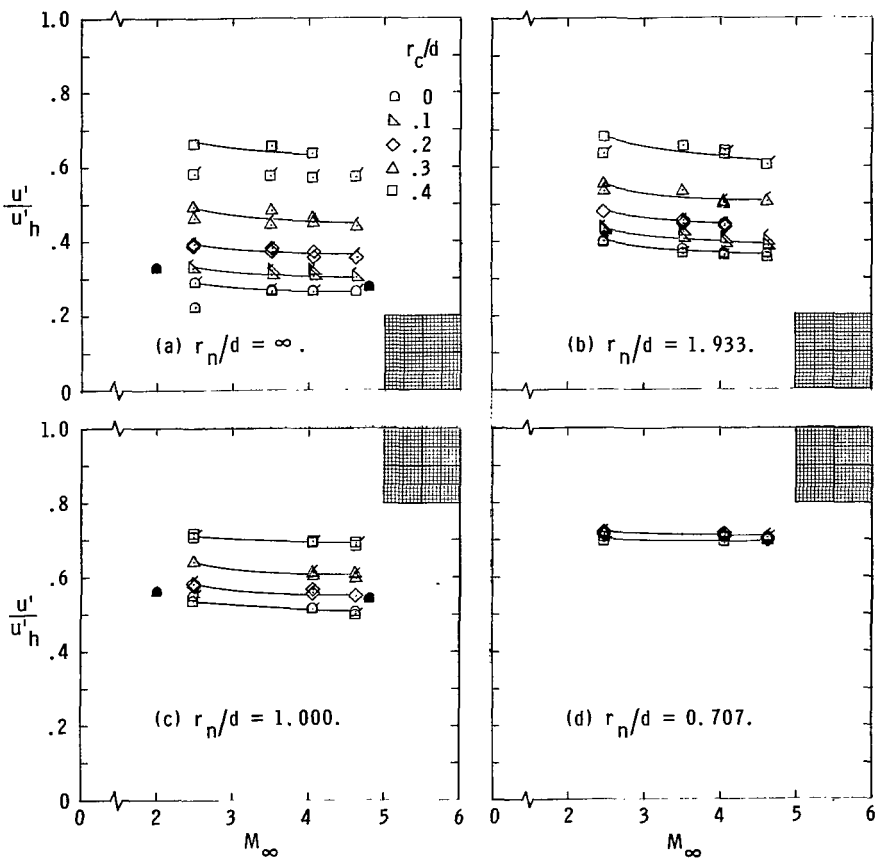

Figure 17.- Variation of stagnation-point velocity gradients with model geometry and Mach number. (Flagged symbols determined from eq. (11); solid symbols from ref. 8.)

of u/u'_h shown in figure 17 were determined from the following equation as derived in appendix B:

$$\frac{u'}{u'_h} = \frac{\delta_h}{\delta} \frac{1 + (\delta/r_n)}{1 + (\delta/r_n)_h} \tag{11}$$

where the values of δ were determined from schlieren photographs and are presented in nondimensional form in figure 18. The values of δ/d shown in figure 18 for $\frac{r_c}{d} = 0.5$ are from previously obtained results for a 9-inch-diameter spherical model tested in the Langley Unitary Plan wind tunnel since schlieren photographs were not obtained for the hemispherical model of the present investigation. Also shown in figure 18 are data from references 25 and 26.

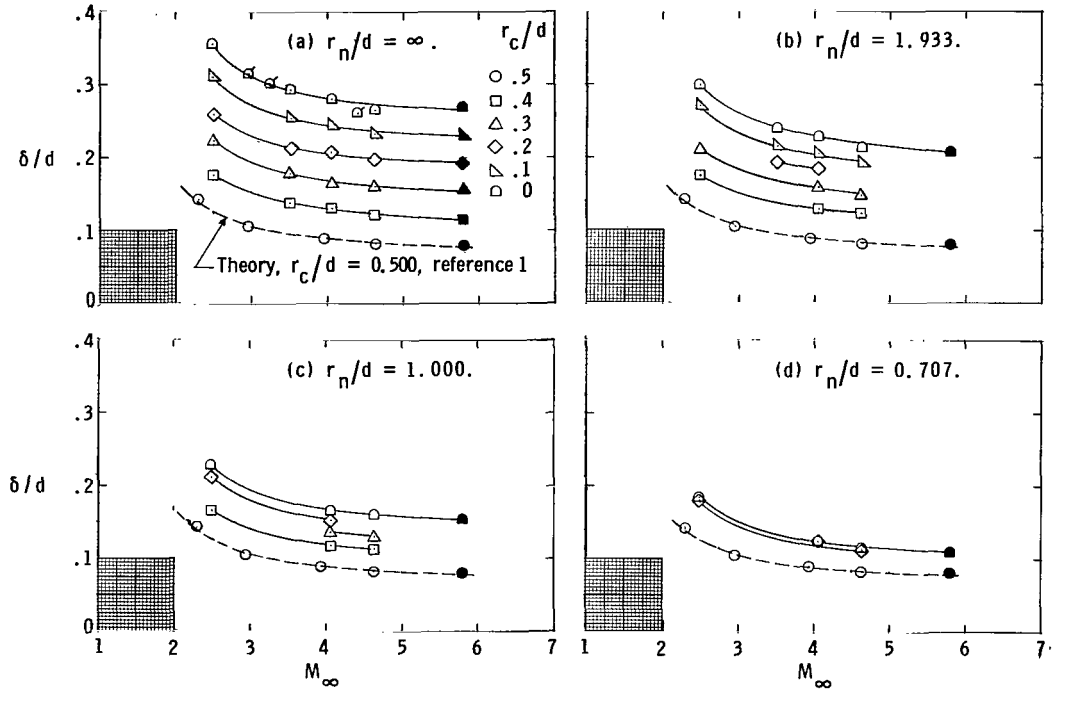

Figure 18.- Variation of shock-standoff distance with model geometry and Mach number. (Solid symbols from ref. 25; flagged symbols from ref. 26.)

In general, the values of u'/u'_h determined from equation (11) are in good agreement with the experimental values. (See fig. 17.) It should be emphasized that u'_h, as used in figure 17 and in all subsequent figures containing the parameter u'/u'_h, corresponds to a hemisphere having a radius equal to the afterbody radius of the general shape depicted in figure 1 and not equal to the nose radius of this general shape.

The nondimensional velocity gradients shown in figure 17 at a Mach number of 4.06 are replotted in figure 19 to show the effect of shoulder radius more clearly. The parameter u'/u'_h is plotted in figure 19 as a function of r_c/d for various values of r_n/d. The advantage of this form of presentation is that for a given Mach number the velocity gradients for this complete family of blunt bodies, ranging from the zero-corner-radius models $\left(\frac{r_c}{d} = 0\right)$ to the hemispherical model $\left(\frac{r_c}{d} = 0.5\right)$, can be shown in one figure for all values of r_n/d. Furthermore, the results in figure 19 should apply to Mach numbers higher than 4.06 because the nondimensional velocity distributions (see fig. 11 as well as fig. 14) are essentially invariant with further increases in Mach number.

The nondimensional velocity gradients shown in figure 17 at a Mach number of 4.06 are replotted in figure 20 to show the effect of nose radius more clearly. The parameter u'/u'_h is plotted as a function of nose radius for various values of r_c/d. In order to retain the data for the flat-face model without using a broken scale, the velocity gradients are plotted as a function of d/r_n rather than the normally used parameter r_n/d. Also shown in figure 20 are the theoretical estimates from modified Newtonian theory (dashed line) and from equation (11) (flagged symbols). The expression for the modified Newtonian theory for this family of bodies reduces to

$$\frac{u'}{u'_h} = \frac{(r_n)_h}{r_n} = \frac{1}{2}\frac{d}{r_n} \tag{12}$$

as can be seen from equation (10). The limited application of the Newtonian theory for predicting stagnation-point velocity gradient for bodies of this type is clearly indicated in figure 20; however, the estimates based on equation (11) are in good agreement with the data throughout the range of geometrical variables.

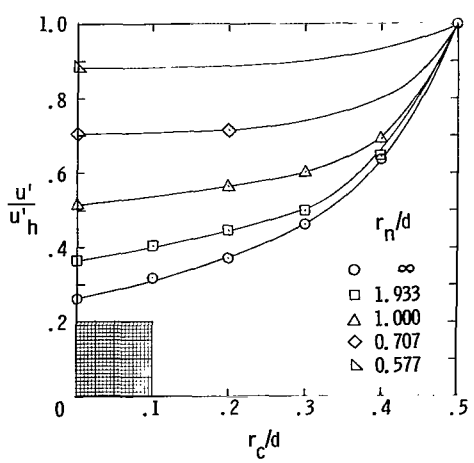

Figure 19.- Effect of shoulder radius on stagnation-point velocity gradients. $M_\infty = 4.06$.

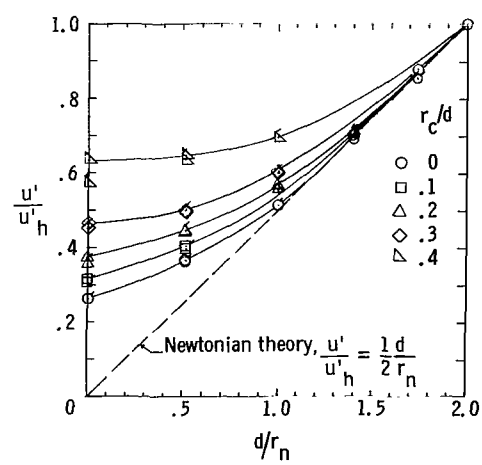

Figure 20.- Effect of nose radius on stagnation-point velocity gradients. $M_\infty = 4.06$. (Flagged symbols denote theoretical values from eq. (11).)

SUMMARY OF RESULTS

Drag coefficients and local flow properties were experimentally determined for a family of blunt bodies at Mach numbers from 2.49 to 4.63. The family consisted of bodies of revolution having variable nose and shoulder radii (r_n and r_c, respectively) and cylindrical afterbodies 7.5 inches (191 mm) in diameter (d). The model geometry ranged from a hemisphere-cylinder $\left(\frac{r_n}{d} = 0.5, \ \frac{r_c}{d} = 0.5\right)$ to a flat-face cylinder $\left(\frac{r_n}{d} = \infty, \ \frac{r_c}{d} = 0\right)$. The results are summarized as follows:

1. The Mach number effect on both the nondimensional pressure distributions and the velocity distributions of the hemispherical model decreased rapidly with increasing Mach number through the Mach number range of this investigation. These distributions at a Mach number of 4.63 were essentially the same as previously published results for Mach numbers up to 11.4.

2. The Mach number effect on the pressure and velocity distributions decreased with increasing the extent of nose bluntness. There was no effect of Mach number on these distributions for the zero-corner-radius models for $\frac{r_n}{d} > 0.707$.

3. Drag coefficients determined from integrated pressures over the nose of the hemispherical model and by assuming the base pressure coefficient to correspond to $-1/M_\infty^2$ (where M_∞ is the free-stream Mach number) were in good agreement with previously published results for a sphere. These results were also in good agreement with drag coefficients determined from pressure distributions evaluated over the model nose by modified Newtonian theory and the use of the aforementioned expression for the base pressure coefficient.

4. A reduction in drag coefficients as indicated by both experiment and theory occurred for a decrease in bluntness obtained by an increase in shoulder radius. The maximum disagreement between experiment and theory was approximately 16 percent and occurred for $\frac{r_n}{d} = \infty$ and $\frac{r_c}{d} = 0.1$ or 0.2. There was essentially no variation in the drag coefficients with Mach number at the higher test Mach numbers.

5. The maximum velocity gradient for all models occurred either at or slightly downstream of the point of tangency of the nose and shoulder arcs.

6. Stagnation-point velocity gradients determined from measured pressures were in very good agreement throughout the range of variables of this investigation with theoretical estimates based on Traugott's method and measured shock-standoff distances.

7. A comprehensive presentation of these data in figure form is included for sufficiently small intervals of nose and shoulder radii to enable the pressure distributions, velocity distributions, stagnation-point velocity gradients, or shock-standoff distances to be determined – either directly or by interpolation – for any body of the general shape

described. Since all these variables indicated only very small Mach number effects at the higher test Mach numbers, these results should be applicable to a much higher range of Mach number than that of this investigation.

Langley Research Center,
National Aeronautics and Space Administration,
Langley Station, Hampton, Va., May 11, 1967,
124-07-02-44-23.

APPENDIX A

NEWTONIAN DRAG COEFFICIENTS

For the family of axisymmetric bodies defined by the geometrical parameters shown in the following sketch:

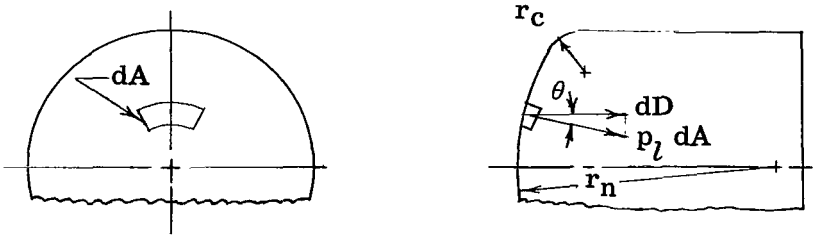

the differential drag resulting from a pressure p_l acting on a differential surface area dA can be expressed as

$$dD = p_l \cos \theta \, dA \tag{A1}$$

The total drag would then become

$$D = \int_A p_l \cos \theta \, dA = \int_{Nose} p_l \cos \theta \, dA + \int_{Base} p_l \cos \theta \, dA \tag{A2}$$

Since the value of θ is constant (180^o) for the base of this family of bodies, the base drag component can be easily integrated if p_b is assumed to be constant. With this assumption, equation (A2) becomes

$$D = \int_{Nose} p_l \cos \theta \, dA - p_b A_b \tag{A3}$$

where A_b is the base area.

In order to present equation (A3) in the form of pressure coefficients, the expression

$$\int_A p_\infty \cos \theta \, dA = 0 \tag{A4}$$

is used in conjunction with equation (A3) to obtain

$$D = \int_{Nose} (p_l - p_\infty) \cos \theta \, dA - (p_b - p_\infty) A_b \tag{A5}$$

In the form of drag coefficient, equation (A5) becomes

$$C_D = \frac{1}{A_b}\int_{Nose} C_p \cos\theta \, dA - C_{p,b} \tag{A6}$$

From modified Newtonian theory, the pressure coefficient can be expressed as

$$C_p = C_{p,max} \cos^2\theta \tag{A7}$$

which when substituted into equation (A6) gives

$$C_D = \frac{C_{p,max}}{A_b}\int_{Nose} \cos^3\theta \, dA - C_{p,b} \tag{A8}$$

The differential area dA for the nose region can be expressed in terms of θ as follows:

For $0 \leqq \theta \leqq \theta_1$,

$$dA = 2\pi r_n^2 \sin\theta \, d\theta \tag{A9a}$$

and for $\theta_1 \leqq \theta \leqq \frac{\pi}{2}$,

$$dA = 2\pi r_c(r_b - r_c + r_c \sin\theta)d\theta \tag{A9b}$$

Combining equations (A8) and (A9) leads to the following integral expression for the drag coefficient:

$$C_D = \frac{C_{p,max}}{A_b} 2\pi r_n^2 \int_0^{\theta_1} \cos^3\theta \sin\theta \, d\theta + \frac{C_{p,max}}{A_b} 2\pi r_c(r_b - r_c)\int_{\theta_1}^{\pi/2} \cos^3\theta \, d\theta$$

$$+ \frac{C_{p,max}}{A_b} 2\pi r_c^2 \int_{\theta_1}^{\pi/2} \cos^3\theta \sin\theta \, d\theta - C_{p,b} \tag{A10}$$

Integrating equation (A10) and rearranging terms yields the following closed-form equation:

$$C_D = \frac{1}{2}\left(\frac{r_n}{r_b}\right)^2 C_{p,max}\left(1 - \cos^4\theta_1\right) + 2C_{p,max}\frac{r_c}{r_b}\left(1 - \frac{r_c}{r_b}\right)\left[\frac{2}{3} - \frac{1}{3}\sin\theta_1\left(\cos^2\theta_1 + 2\right)\right]$$

$$+ \frac{1}{2} C_{p,max}\left(\frac{r_c}{r_b}\right)^2 \cos^4\theta_1 - C_{p,b} \qquad \left(\frac{r_n}{r_b} < \infty\right) \tag{A11}$$

This equation is of indeterminate form for $\frac{r_n}{r_b} = \infty$; however, by taking the appropriate limiting process, it can easily be reduced to the following form:

$$C_D = C_{p,max}\left(1 - \frac{r_c}{r_b}\right)^2 + \frac{4}{3} C_{p,max} \frac{r_c}{r_b}\left(1 - \frac{r_c}{r_b}\right) + \frac{1}{2} C_{p,max}\left(\frac{r_c}{r_b}\right)^2 - C_{p,b} \qquad \left(\frac{r_n}{r_b} = \infty\right) \quad \text{(A12)}$$

APPENDIX B

NONDIMENSIONAL STAGNATION-POINT VELOCITY GRADIENTS

Using the first Belotserkovskii approximation, Traugott (ref. 5) obtained simple analytical relations for the stagnation region of blunt bodies between shock and body curvature, shock-standoff distance, and velocity gradient. These relations enable an approximation of stagnation-point velocity gradients to be made from optical information, which is generally much easier to obtain than pressure data. The equation from reference 5 relating stagnation-point velocity gradient with shock-standoff distance is

$$\frac{1}{u_\infty}\left[\frac{\delta}{1 + (\delta/r_n)}\right]u' = \pi(M_\infty,\gamma) \tag{B1}$$

where

$$\pi(M_\infty,\gamma) = \frac{2 + (\gamma - 1)M_\infty^2}{(\gamma + 1)M_\infty^2}\left\{1 - \Gamma\left[\frac{2\left(M_\infty^2 - 1\right)}{2 + (\gamma - 1)M_\infty^2}\right]\right\}\left[\frac{4\gamma M_\infty^2 - 2(\gamma - 1)}{(\gamma + 1)^2 M_\infty^2}\right]^{1/(\gamma-1)}$$

and

$$\Gamma(M_\infty,\gamma) = \frac{2(\gamma + 1) + 2\gamma(\gamma + 1)M_\infty^2 - (\gamma + 1)^2 M_\infty^2\left\{(\gamma + 1)^2 M_\infty^2 \Big/ \left[4\gamma M_\infty^2 - 2(\gamma - 1)\right]\right\}^{1/(\gamma-1)}}{4\gamma\left(M_\infty^2 - 1\right)}$$

Since both π and Γ are independent of model geometry, they can be eliminated from equation (B1) by nondimensionalizing the stagnation-point velocity gradient by the gradient for some reference shape. A logical shape to use is the hemisphere since both the stagnation-point velocity gradient and shock-standoff distance are well defined through a wide range of Mach number. Solving equation (B1) for u' and nondimensionalizing by u'_h gives

$$\frac{u'}{u'_h} = \frac{\delta_h}{\delta}\,\frac{1 + (\delta/r_n)}{1 + (\delta/r_n)_h} \tag{B2}$$

which is applicable for any value of M_∞ or γ.

REFERENCES

1. Van Dyke, Milton D.; and Gordon, Helen D.: Supersonic Flow Past a Family of Blunt Axisymmetric Bodies. NASA TR R-1, 1959.

2. Inouye, Mamoru: Blunt Body Solutions for Spheres and Ellipsoids in Equilibrium Gas Mixtures. NASA TN D-2780, 1965.

3. Lomax, Harvard; and Inouye, Mamoru: Numerical Analysis of Flow Properties About Blunt Bodies Moving at Supersonic Speeds in an Equilibrium Gas. NASA TR R-204, 1964.

4. Belotserkovskii, O. M.: Flow Past a Circular Cylinder With a Detached Shock Wave. Tech. Memo. RAD-9-TM-59-66, AVCO Res. and Advance Dev. Div., Sept. 30, 1959.

5. Traugott, Stephen C.: An Approximate Solution of the Direct Supersonic Blunt-Body Problem for Arbitrary Axisymmetric Shapes. J. Aerospace Sci., vol. 27, no. 5, May 1960, pp. 361-370.

6. Swigart, Rudolph J.: A Theory of Asymmetric Hypersonic Blunt-Body Flows. AIAA J., vol. 1, no. 5, May 1963, pp. 1034-1042.

7. Perry, James C.; and Pasiuk, Lionel: A Comparison of Solutions to a Blunt Body Problem. AIAA J. (Tech. Notes), vol. 4, no. 8, Aug. 1966, pp. 1425-1426.

8. Boison, J. Christopher; and Curtiss, Howard A.: An Experimental Investigation of Blunt Body Stagnation Point Velocity Gradient. ARS J., vol. 29, no. 2, Feb. 1959, pp. 130-135.

9. Zoby, Ernest V.; and Sullivan, Edward M.: Effects of Corner Radius on Stagnation-Point Velocity Gradients on Blunt Axisymmetric Bodies. NASA TM X-1067, 1965.

10. Cooper, Morton; and Mayo, Edward E.: Measurements of Local Heat Transfer and Pressures on Six 2-Inch-Diameter Blunt Bodies at a Mach Number of 4.95 and at Reynolds Numbers Per Foot up to 81×10^6. NASA MEMO 1-3-59L, 1959.

11. Lawson, Warren A.; McDearmon, R. W.; and Rainey, R. W.: Investigation of the Pressure Distributions on Reentry Nose Shapes at a Mach Number of 3.55. NASA TM X-244, 1960.

12. Anon.: Manual for Users of the Unitary Plan Wind Tunnel Facilities of the National Advisory Committee for Aeronautics. NACA, 1956.

13. Bertram, Mitchel H.; and Everhart, Phillip E.: An Experimental Study of the Pressure and Heat-Transfer Distribution on a 70° Sweep Slab Delta Wing in Hypersonic Flow. NASA TR R-153, 1963.

14. Dunavant, James C.; and Stone, Howard W.: Effect of Roughness on Heat Transfer to Hemisphere Cylinders at Mach Numbers 10.4 and 11.4. NASA TN D-3871, 1967.

15. Charters, A. C.; and Thomas,R. N.: The Aerodynamic Performance of Small Spheres From Subsonic to High Supersonic Velocities. J. Aeron. Sci., vol. 12, no. 4, Oct. 1945, pp. 468-476.

16. Clark, A. B. J.; and Harris, Fred T. (With appendix by R. E. Roberson): Free-Flight Air-Drag Measurement Techniques. NRL Rep. 3727, Naval Res. Lab., Sept. 6, 1950.

17. Hodges, A. J.: The Drag Coefficient of Very High Velocity Spheres. J. Aeron. Sci., vol. 24, no. 10, Oct. 1957, pp. 755-758.

18. Penland, Jim A.: Aerodynamic Characteristics of a Circular Cylinder at Mach Number 6.86 and Angles of Attack up to 90^{o}. NACA TN 3861, 1957. (Supersedes NACA RM L54A14.)

19. Crawford, Davis H.; and McCauley, William D.: Investigation of the Laminar Aerodynamic Heat-Transfer Characteristics of a Hemisphere-Cylinder in the Langley 11-Inch Hypersonic Tunnel at a Mach Number of 6.8. NACA Rept. 1323, 1957. (Supersedes NACA TN 3706.)

20. Stine, Howard A.; and Wanlass, Kent: Theoretical and Experimental Investigation of Aerodynamic-Heating and Isothermal Heat-Transfer Parameters on a Hemispherical Nose With Laminar Boundary Layer at Supersonic Mach Numbers. NACA TN 3344, 1954.

21. Korobkin, Irving: Local Flow Conditions, Recovery Factors, and Heat-Transfer Coefficients on the Nose of a Hemisphere-Cylinder at a Mach Number of 2.8. NAVORD Rept. 2865 (Aeroballistic Res. Rept. 175), U.S. Naval Ord. Lab. (White Oak, Md.), May 5, 1953.

22. Stalder, Jackson R.; and Neilsen, Helmer V.: Heat Transfer From a Hemisphere-Cylinder Equipped With Flow-Separation Spikes. NACA TN 3287, 1954.

23. Korobkin, Irving: Laminar Heat Transfer Characteristics of a Hemisphere for the Mach Number Range 1.9 to 4.9. NAVORD Rept. 3841 (Aeroballistic Res. Rept. 257), U.S. Naval Ord. Lab. (White Oak, Md.), Oct. 10, 1954.

24. Oliver, Robert E.: An Experimental Investigation of Flow Over Simple Blunt Bodies at a Nominal Mach Number of 5.8. GALCIT Memo. No. 26 (Contract No. DA-04-495-Ord-19), June 1, 1955.

25. Lees, Lester: Recent Developments in Hypersonic Flow. Jet Propulsion, vol. 27, no. 11, Nov. 1957, pp. 1162-1178.

26. Serbin, Hyman: Supersonic Flow Around Blunt Bodies. J. Aeron. Sci. (Readers' Forum), vol. 25, no. 1, Jan. 1958, pp. 58-59.

NASA-Langley, 1967 —— 12 L-5454

"The aeronautical and space activities of the United States shall be conducted so as to contribute . . . to the expansion of human knowledge of phenomena in the atmosphere and space. The Administration shall provide for the widest practicable and appropriate dissemination of information concerning its activities and the results thereof."

—NATIONAL AERONAUTICS AND SPACE ACT OF 1958

NASA SCIENTIFIC AND TECHNICAL PUBLICATIONS

TECHNICAL REPORTS: Scientific and technical information considered important, complete, and a lasting contribution to existing knowledge.

TECHNICAL NOTES: Information less broad in scope but nevertheless of importance as a contribution to existing knowledge.

TECHNICAL MEMORANDUMS: Information receiving limited distribution because of preliminary data, security classification, or other reasons.

CONTRACTOR REPORTS: Scientific and technical information generated under a NASA contract or grant and considered an important contribution to existing knowledge.

TECHNICAL TRANSLATIONS: Information published in a foreign language considered to merit NASA distribution in English.

SPECIAL PUBLICATIONS: Information derived from or of value to NASA activities. Publications include conference proceedings, monographs, data compilations, handbooks, sourcebooks, and special bibliographies.

TECHNOLOGY UTILIZATION PUBLICATIONS: Information on technology used by NASA that may be of particular interest in commercial and other non-aerospace applications. Publications include Tech Briefs, Technology Utilization Reports and Notes, and Technology Surveys.

Details on the availability of these publications may be obtained from:

SCIENTIFIC AND TECHNICAL INFORMATION DIVISION

NATIONAL AERONAUTICS AND SPACE ADMINISTRATION

Washington, D.C. 20546